

Topological linear magnetoresistivity and thermoconductivity induced by noncentrosymmetric Berry curvature

Min-Xue Yang,^{1,*} Hai-Dong Li,^{1,*} Wei Luo,^{1,2} Bingfeng Miao,¹ Wei Chen,^{1,†} and D. Y. Xing¹

¹National Laboratory of Solid State Microstructures, School of Physics,
and Collaborative Innovation Center of Advanced Microstructures, Nanjing University, Nanjing 210093, China
²School of Science, Jiangxi University of Science and Technology, Ganzhou 341000, China

The Berry curvature plays a key role in the magnetic transport of topological materials. Yet, it is not clear whether the Berry curvature by itself can give rise to universal transport phenomena with specific scaling behaviors. In this work, based on the semiclassical Boltzmann formalism and the symmetry analysis, we show that the noncentrosymmetric distribution of the Berry curvature generally results in linear magnetoresistivity and thermoconductivity both exhibiting the B -scaling behavior. We then study such kind of topological linear magnetoresistivity in the 2D MnBi_2Te_4 flakes and the 3D spin-orbit-coupled electron gas, the former showing good agreement with the experimental observations. The difference between our mechanism and the conventional anisotropic magnetoresistance is elucidated. Our theory proposes a universal scenario for the topological linear magnetoresistivity and thermoconductivity and predicts such effects to occur in various materials, which also provides a reasonable explanation for the recent observations of linear magnetoresistivity.

I. INTRODUCTION

The magnetic field effect on electron dynamics is an important manifestation of the electron properties, which can be probed by the transport measurements of the magnetoresistivity (MR) [1]. There are a variety of physical scenarios for the MR, which can usually be discriminated by their specific scaling behaviors in the magnetic field B . For example, the conventional positive magnetoresistance in metal possesses a B^2 -scaling [2] and the weak localization effect results in the dimension-dependent scaling behaviors of the MR with the $\ln B$ -scaling for 2D diffusion and \sqrt{B} -scaling for 3D diffusion, respectively [3]. In the past two decades, the study on topological materials [4–6] shows that the band topology introduces new ingredients to the MR scenarios. For example, the chiral anomaly and Berry curvature effect can induce negative MR with B^2 -scaling in Weyl semimetals [7, 8] and the nontrivial Berry phase results in a sign change of the MR in topological insulators and topological semimetals [9–13], etc.

Different from the scaling laws mentioned above, there also exist several scenarios which can give rise to linear MR (LMR) [12, 14–34]. In particular, there are two types of LMR in the literature which are proportional to B and $|B|$, respectively. In the former case, the MR changes its sign as B is inverted and so exhibits non-reciprocity while in the latter case, the sign of the MR remains the same despite the inversion of B . Away from the quantum limit [12, 21, 27, 30, 31], the LMR with B -scaling may originate from the chiral scattering and self-field effect [14], chiral anomaly [17], spin-orbit coupling and ferromagnetic momentum-dependent exchange interaction [15], intravalley-scattering effects [16], and

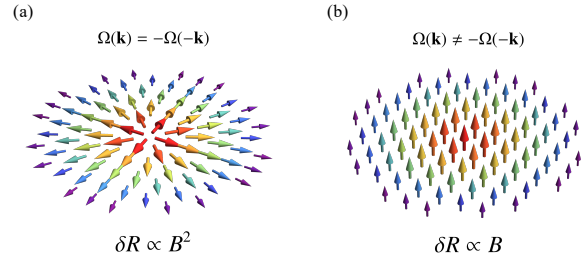


FIG. 1. (Color online). Sketch of the (a) centrosymmetric and (b) noncentrosymmetric distributions of the Berry curvature, which give rise to the magnetoresistivity with B^2 -scaling and B -scaling, respectively.

complex spin configurations [34], etc; Moreover, the MR with $|B|$ -dependence is also observed in several experiments [24, 32, 35], which are attributed to the disorder-induced mobility fluctuation [26, 35] and the shift of the Fermi surface [24, 32]. As one can see, different from other types of scaling laws which are pertinent to certain mechanisms, the LMR can arise due to a variety of physical origins. On the one hand, the phenomena associated with the LMR indicate rich underlying physics; On the other hand, it becomes extremely challenging to discriminate different scenarios from each other in the experiments.

In this work, we uncover a new and general mechanism for the nonreciprocal LMR with B -scaling, dubbed *topological LMR* (TLMR). It arises due to the noncentrosymmetric distribution of the Berry curvature of the energy bands in the reciprocal space; see Fig. 1. In the semiclassical transport regime, the effects due to the Berry curvature mainly originate from two aspects, the anomalous velocities [36] and the correction to the density of states (DOS) [37, 38]. It gives rise to several exotic magneto-transport phenomena such as the anomalous

* The authors contribute equally.

† Corresponding author: pchenweis@gmail.com

Hall effect [36, 39], the negative MR in Weyl semimetals and topological insulators [7, 8, 40], and the chiral magnetic effect [41–43], etc. It was also discovered in some specific systems that the Berry curvature effect can lead to nonreciprocal LMR [18–20]. Yet, whether there exists a general mechanism for the TLMR induced by the Berry curvature remains an open question.

In this work, based on the semiclassical Boltzmann formalism and symmetry analysis, we show that the noncentrosymmetric distribution of the Berry curvature in the reciprocal space can generally give rise to the TLMR and similar topological linear thermoconductivity (TLTC) with B -scaling in both 2D and 3D systems. We exemplify the general mechanism with two physical systems: the 2D flakes of topological material MnBi_2Te_4 [22] and 3D electron gas with the Rashba or Dresselhaus spin-orbit coupling and a magnetic order [44]. For the former case, the results calculated by our theory are in good agreement with the observations in the transport experiment on the MnBi_2Te_4 flakes [22]; Meanwhile, we predict the TLMR effect in the 3D electron gas with spin-orbit coupling and leave it to be explored in future experiments. Given that the main ingredient, noncentrosymmetric distributed Berry curvature is ubiquitous, the TLMR and TLTC effects are expected to exist in various systems with nonvanishing Berry curvature.

The rest of the paper is organized as follows. The semiclassical transport theory is briefly introduced in Sec. II. In Sec. III, a symmetry analysis on the occurrence of the TLMR is given. Then the TLMR in the topological material MnBi_2Te_4 is studied and the results are compared with the experimental observations in Sec. IV. In Sec. V, we predict the TLMR to arise in the 3D spin-orbit coupled electron gas with a magnetic order. In Sec. VI, we discuss the phenomena associated with the multi-domain structures and compare our scenario with that of the conventional anisotropic magnetoresistance. The effect of the TLTC is discussed in Sec. VII. Finally, some concluding remarks are given in Sec. VIII.

II. SEMICLASSICAL TRANSPORT THEORY

We consider the magnetic transport in the diffusive regime and describe it by the semiclassical Boltzmann formalism. For a weak magnetic field such that the electron cannot achieve the entire cyclotron motion along the closed orbit before getting scattered, the effect due to the Landau levels can be neglected. The semiclassical equations of motion for the electron in the energy bands with nonvanishing Berry curvature read [36, 45]

$$\dot{\mathbf{r}} = \frac{1}{\hbar} \nabla_{\mathbf{k}} \epsilon_{\mathbf{k}} - \dot{\mathbf{k}} \times \boldsymbol{\Omega}_{\mathbf{k}}, \quad \dot{\mathbf{k}} = -\frac{e}{\hbar} (\mathbf{E} + \dot{\mathbf{r}} \times \mathbf{B}), \quad (1)$$

where \mathbf{r} and \mathbf{k} are the center position and momentum of the wave packet, respectively, $\boldsymbol{\Omega}_{\mathbf{k}} = i \langle \nabla_{\mathbf{k}} u_{\mathbf{k}} | \times | \nabla_{\mathbf{k}} u_{\mathbf{k}} \rangle$ is the Berry curvature defined by the wave functions $|u_{\mathbf{k}}\rangle$,

$\epsilon_{\mathbf{k}}$ is the energy, \mathbf{E} (\mathbf{B}) are the external electric (magnetic) field and \hbar is the reduced Planck constant.

In the linear response regime, the effective velocity can be solved as (taking $\mathbf{E} = 0$)

$$\dot{\mathbf{r}} = [\mathbf{v}_{\mathbf{k}} + (e/\hbar) \mathbf{B} (\mathbf{v}_{\mathbf{k}} \cdot \boldsymbol{\Omega}_{\mathbf{k}})] / D_{\mathbf{k}}, \quad (2)$$

where $\mathbf{v}_{\mathbf{k}} = (1/\hbar) \nabla_{\mathbf{k}} \epsilon_{\mathbf{k}}$ is the group velocity and $D_{\mathbf{k}}$ is the correction to the DOS [37, 38] with

$$D_{\mathbf{k}} = 1 + \frac{e}{\hbar} \mathbf{B} \cdot \boldsymbol{\Omega}_{\mathbf{k}}. \quad (3)$$

Similarly, the time derivative of the momentum is

$$\dot{\mathbf{k}} = -\frac{e}{\hbar D_{\mathbf{k}}} [\mathbf{E} + \mathbf{v}_{\mathbf{k}} \times \mathbf{B} + \frac{e}{\hbar} (\mathbf{B} \cdot \mathbf{E}) \boldsymbol{\Omega}_{\mathbf{k}}]. \quad (4)$$

We employ the relaxation time approximation and make the assumption that various scattering processes are independent. This enables us to employ the Matthiessen's rule $1/\tau = \sum_{i=1}^3 1/\tau_i$ [46], in which three main scenarios that dominate the transport are the scattering due to the impurity, electron-electron interaction and phonon, characterized by the relaxation time τ_1 , τ_2 and τ_3 , respectively. Under the uniform and steady-state condition, the semiclassical Boltzmann equation reduces to

$$\dot{\mathbf{k}} \cdot \nabla_{\mathbf{k}} f = -\frac{f - f_0}{\tau}, \quad (5)$$

where f is the actual distribution function of electrons under the action of the external fields and $f_0 = 1/[e^{(\epsilon_{\mathbf{k}} - \epsilon_F)/k_B T} + 1]$ is the Fermi-Dirac function in equilibrium with a Fermi energy ϵ_F . By combining Eq. (4) and Eq. (5), the distribution function deviated from the equilibrium to the first-order of \mathbf{E} can be obtained as

$$f_1 = \frac{e\tau}{D_{\mathbf{k}}} [\mathbf{E} + \frac{e}{\hbar} (\mathbf{E} \cdot \mathbf{B}) \boldsymbol{\Omega}_{\mathbf{k}}] \cdot \mathbf{v}_{\mathbf{k}} \frac{\partial f_0}{\partial \epsilon_{\mathbf{k}}}. \quad (6)$$

It gives rise to a finite current density with $D_{\mathbf{k}}$ is the correction to the DOS

$$\mathbf{J} = -e \int \frac{d^3 \mathbf{k}}{(2\pi)^3} f_1 D_{\mathbf{k}} \dot{\mathbf{r}}. \quad (7)$$

By inserting Eqs. (2) and (6) into the current expression, the longitudinal conductivity $\sigma_{\mu\mu}$ defined by $J_{\mu} = \sigma_{\mu\mu} E_{\mu}$ ($\mu = x, y, z$) can be obtained as

$$\sigma_{\mu\mu} = -\frac{e^2 \tau}{(2\pi)^3} \int \frac{d^3 \mathbf{k}}{D_{\mathbf{k}}} (v_{\mathbf{k}}^{\mu} + \frac{e}{\hbar} B^{\mu} \mathbf{v}_{\mathbf{k}} \cdot \boldsymbol{\Omega}_{\mathbf{k}})^2 \frac{\partial f_0}{\partial \epsilon_{\mathbf{k}}}. \quad (8)$$

III. SYMMETRY ANALYSIS ON THE TLMR

The general condition for the occurrence of the TLMR (as well as the TLTC to be discussed in Sec. VII) can already be drawn from Eq. (8) through the symmetry analysis without going into details about the systems,

which reflects the universality of the present scenario of the TLMR. To see this, we expand Eq. (8) to the first order in \mathbf{B} as

$$\sigma_{\mu\mu}^{(1)} = \frac{e^3\tau}{(2\pi)^3\hbar} \int d^3\mathbf{k} v_{\mathbf{k}}^\mu [v_{\mathbf{k}}^\mu (\mathbf{B} \cdot \boldsymbol{\Omega}_{\mathbf{k}}) - 2B^\mu (\mathbf{v}_{\mathbf{k}} \cdot \boldsymbol{\Omega}_{\mathbf{k}})] \frac{\partial f_0}{\partial \epsilon_{\mathbf{k}}}, \quad (9)$$

where the two terms inside the square parenthesis come from the DOS correction $D_{\mathbf{k}}$ in Eq. (3) and the anomalous velocity in Eq. (2), respectively. The expression contains the integral over the Berry curvature $\boldsymbol{\Omega}_{\mathbf{k}}$ around the Fermi surface, which can be regarded as a fictitious magnetic field in the reciprocal space. The TLMR takes place as $\sigma_{\mu\mu}^{(1)}$ possesses a finite value.

The symmetry restriction on the distribution of the Berry curvature has a strong impact on $\sigma_{\mu\mu}^{(1)}$. Specifically, in the presence of the time-reversal symmetry, the Berry curvature satisfies [36]

$$\boldsymbol{\Omega}_{\mathbf{k}} = -\boldsymbol{\Omega}_{-\mathbf{k}}, \quad (10)$$

meaning a centrosymmetric distribution of the vector field in the momentum space as shown in Fig. 1(a). Note that the inversion operation reverses both the wave vector \mathbf{k} and the vector field $\boldsymbol{\Omega}_{\mathbf{k}}$. Then the integrals of both two terms in Eq. (8) vanish given that the velocity also obeys $\mathbf{v}_{\mathbf{k}} = -\mathbf{v}_{-\mathbf{k}}$ due to the time reversal symmetry which stems from $\epsilon_{\mathbf{k}} = \epsilon_{-\mathbf{k}}$. In this case, the magnetoconductivity (as well as the MR) to the lowest-order in B is $\propto B^2$ meaning the absence of the TLMR. Such negative quadratic MR has been proposed theoretically [7, 8] and confirmed experimentally [47, 48] in Weyl semimetals, in which the centrosymmetric distribution of $\boldsymbol{\Omega}_{\mathbf{k}}$ sketched in Fig. 1(a) is satisfied for each Weyl cone although the whole system may not have the time-reversal symmetry. This case can be understood as a time-reversal-like antiunitary symmetry defined locally at each Weyl cone.

From the symmetry analysis above, one can see that the noncentrosymmetric distribution of the Berry curvature like that in Fig. 1(b), and the underlying symmetry restriction on the system are essential for the TLMR. It should be noted that mathematically, the noncentrosymmetric structures of both $\boldsymbol{\Omega}_{\mathbf{k}}$ and $\mathbf{v}_{\mathbf{k}}$ do not necessarily ensure the occurrence of the LMR because the integral in Eq. (9) exhibits a complex dependence on both $\boldsymbol{\Omega}_{\mathbf{k}}$ and $\mathbf{v}_{\mathbf{k}}$. In reality, however, it is reasonable to expect a finite $\sigma_{\mu\mu}^{(1)}$ in case that the system has no symmetry restriction on $\boldsymbol{\Omega}_{\mathbf{k}}$ and $\mathbf{v}_{\mathbf{k}}$.

Furthermore, we show that the conclusion above maintains even the effect due to the orbital magnetic moment is taken into account. That is, in the system with time-reversal(-like) symmetry, neither Berry curvature nor orbit magnetic moment will induce TLMR. The orbit magnetic moment originates from the self-rotation of the wave packet [36, 49] and takes the form of

$$\mathcal{M}_{\mathbf{k}} = -i \frac{e}{2\hbar} \langle \nabla_{\mathbf{k}} u_{\mathbf{k}} | \times [H(\mathbf{k}) - \epsilon(\mathbf{k})] | \nabla_{\mathbf{k}} u_{\mathbf{k}} \rangle. \quad (11)$$

where $H(\mathbf{k}) = e^{-i\mathbf{k}\cdot\mathbf{r}} H e^{i\mathbf{k}\cdot\mathbf{r}}$ is the Bloch Hamiltonian. Its coupling to the external magnetic field \mathbf{B} results in

a Zeeman-like term and the energy becomes $\tilde{\epsilon}_{\mathbf{k}} = \epsilon_{\mathbf{k}} - \mathcal{M}_{\mathbf{k}} \cdot \mathbf{B}$, which modifies the group velocity of the electron to $\tilde{\mathbf{v}}_{\mathbf{k}} = \mathbf{v}_{\mathbf{k}} - \delta\mathbf{v}_{\mathbf{k}}$ with $\delta\mathbf{v}_{\mathbf{k}} = \nabla_{\mathbf{k}}(\mathcal{M}_{\mathbf{k}} \cdot \mathbf{B})/\hbar$. As a result, the longitudinal conductivity in Eq. (8) changes into [40, 50, 51]

$$\tilde{\sigma}_{\mu\mu} = - \int \frac{d^3\mathbf{k}}{(2\pi)^3} \frac{e^2\tau}{D_{\mathbf{k}}} (\tilde{v}_{\mathbf{k}}^\mu + \frac{e}{\hbar} B^\mu \tilde{\mathbf{v}}_{\mathbf{k}} \cdot \boldsymbol{\Omega}_{\mathbf{k}})^2 \frac{\partial f_0}{\partial \tilde{\epsilon}_{\mathbf{k}}}. \quad (12)$$

It can be proved that $\mathcal{M}_{\mathbf{k}}$ possesses the same symmetry as that of the Berry curvature if the system possesses the time-reversal(-like) symmetry, i.e.,

$$\mathcal{M}_{\mathbf{k}} = -\mathcal{M}_{-\mathbf{k}}, \quad (13)$$

given that the former is induced by the latter. Thus, we have $\delta\mathbf{v}_{\mathbf{k}} = \delta\mathbf{v}_{-\mathbf{k}}$. The effect due to the orbital magnetic moment contributes additional terms to Eq. (9) as

$$\delta\sigma_{\mu\mu}^{(1)} = \int \frac{d^3\mathbf{k}}{(2\pi)^3} e^2\tau [v_{\mathbf{k}}^\mu \delta v_{\mathbf{k}}^\mu \frac{\partial f_0}{\partial \epsilon_{\mathbf{k}}} + (v_{\mathbf{k}}^\mu)^2 (\mathcal{M}_{\mathbf{k}} \cdot \mathbf{B}) \frac{\partial^2 f_0}{\partial \epsilon_{\mathbf{k}}^2}] \quad (14)$$

However, such terms vanish as well due to the symmetry restriction $\mathcal{M}_{\mathbf{k}} = -\mathcal{M}_{-\mathbf{k}}$, $\delta\mathbf{v}_{\mathbf{k}} = \delta\mathbf{v}_{-\mathbf{k}}$ and $\mathbf{v}_{\mathbf{k}} = -\mathbf{v}_{-\mathbf{k}}$. Therefore, the inclusion of the effect due to the orbital magnetic moment does not change our conclusion, that is, the noncentrosymmetric distribution of the Berry curvature is key to the TLMR.

The aforementioned scenario of the TLMR is quite general and is expected to exist in a variety of materials with nonvanishing Berry curvature distribution, no matter in 2D or 3D. It does not even require the whole Bloch bands to be topologically nontrivial, because only the Berry curvature of the states near the Fermi energy dominates the effect. Here, we would like to point out that although the noncentrosymmetric distribution of the Berry curvature provides a general scenario for the TLMR, it is not a necessary condition for it. From Eq. (9), the LMR can also occur under the condition $\boldsymbol{\Omega}_{\mathbf{k}} = -\boldsymbol{\Omega}_{-\mathbf{k}}$ and $\mathbf{v}_{\mathbf{k}} \neq -\mathbf{v}_{-\mathbf{k}}$, of which a typical example is the type II Weyl semimetal [18, 19]. Such a scenario is not the focus of this work. For clarification, we compare different scenarios of the MR due to the Berry curvature effect in table I.

To show the universality of the noncentrosymmetric Berry curvature induced TLMR, in the following sections, we will study the TLMR in two specific systems, the 2D MnBi₂Te₄ flakes and the 3D spin-orbit coupled electron gas. The generalization of our theory to other systems is straightforward.

IV. TLMR IN 2D MnBi₂Te₄ FLAKES

We first consider the 2D material MnBi₂Te₄, which is the first discovered intrinsic magnetic topological insulator that exhibits quantum anomalous Hall effect and has sparked a surge of research interest [22, 53–55]. One

$\Omega_{\mathbf{k}} = -\Omega_{-\mathbf{k}}$	$\mathbf{v}_{\mathbf{k}} = -\mathbf{v}_{-\mathbf{k}}$	B -Scaling of MR	Examples
\times	$\times(\checkmark)$	B	MnBi ₂ Te ₄ in Sec IV, electron gas in Sec V, magnetic Weyl semimetal [20]
\checkmark	\times	B	Type-II Weyl [18, 19]
\checkmark	\checkmark	B^2	Type-I Weyl, etc [52]

TABLE I. Symmetry conditions and the corresponding B -scaling of the MR. The last column shows typical examples.

unique feature of the 2D systems is that the Berry curvature possesses only the z -component so that the MR originates solely from its coupling to the B_z component of the magnetic field. Because the electron transport takes place within the 2D plane, the in-plane velocity and the out-of-plane Berry curvature ensures $\mathbf{v}_{\mathbf{k}} \cdot \Omega_{\mathbf{k}} = 0$ in Eq. (2), *i.e.*, the absence of the anomalous velocity. Therefore, the MR stems entirely from the DOS correction $D_{\mathbf{k}}$ induced by the Berry curvature according to Eq. (8).

The LMR with B -scaling has been observed in the transition region between the two opposite quantum anomalous Hall plateaus; see Fig. 2 of Ref. [22]. In this region, the nonvanishing longitudinal resistance indicates the participation of the bulk states in the transport. Out side of the transition region, the Fermi energy should lie in the gap between the conduction and valence bands. We here employ the effective Hamiltonian of the MnBi₂Te₄ flakes [22, 56]

$$H_{\text{MBT}} = \begin{pmatrix} \Delta + m_{\mathbf{k}} & ivk_- & 0 & 0 \\ -ivk_+ & -\Delta - m_{\mathbf{k}} & 0 & 0 \\ 0 & 0 & -\Delta + m_{\mathbf{k}} & -ivk_+ \\ 0 & 0 & ivk_- & \Delta - m_{\mathbf{k}} \end{pmatrix}, \quad (15)$$

where v is the velocity of the surface states, $k_{\pm} = k_x \pm ik_y$ is defined by the 2D wave vectors, $m_{\mathbf{k}} = m_0 + m_1(k_x^2 + k_y^2)$ captures the tunneling effect between the top and bottom surface states with m_0, m_1 the relevant parameters, and Δ is the exchange field along the z -direction due to the ferromagnetic order. Whether the Dirac mass is inverted or not at the Γ point determines the Chern number \mathcal{C} of the valence bands and specifically, $\mathcal{C} = 0$ for $|\Delta| < |m_0|$ and $\mathcal{C} = \text{sgn}(\Delta)$ for $|\Delta| > |m_0|$, respectively [22]. By diagonalizing the Hamiltonian H_{MBT} , we obtain four bands with dispersions $\epsilon_u^{\pm} = \pm\sqrt{(\Delta + m_{\mathbf{k}})^2 + v^2k^2}$, $\epsilon_l^{\pm} = \pm\sqrt{(\Delta - m_{\mathbf{k}})^2 + v^2k^2}$, where the subscripts u, l denote the upper and lower blocks of Eq. (15), respectively.

To involve the bulk contribution to the longitudinal transport as was observed in the experiment, we consider the Fermi energy ϵ_F intersects the upper valence band in the transition region as illustrated in Fig. 2(a). In particular, the upper valence band is referred to ϵ_l^- and ϵ_u^- for $\Delta > 0$ and $\Delta < 0$, with the corresponding eigenstates $|v_l^-\rangle = [0, 0, -ivk_+, -2\sqrt{(\Delta - m_{\mathbf{k}})^2 + v^2k^2} \sin^2 \theta_l]^T / N_l$ and $|v_u^-\rangle = [ivk_-, -2\sqrt{(\Delta + m_{\mathbf{k}})^2 + v^2k^2} \cos^2 \theta_u, 0, 0]^T / N_u$, respectively, whose normalization factors

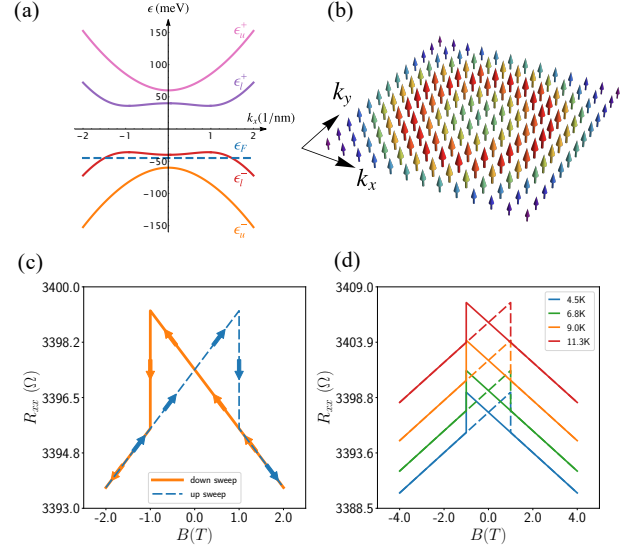


FIG. 2. (Color online). (a) Energy spectra of the surface state of MnBi₂Te₄ ($k_y = 0$). The dashed blue line represents the position of the Fermi energy. (b) The distribution of the Berry curvature of MnBi₂Te₄. (c) The TLMR as a function of the magnetic field at $T = 1.2$ K. The arrowed dashed line represents the up sweep and the arrowed solid line represents the down sweep. (d) TLMR at different temperatures. The relevant parameters are $\tau = 10^{-12}$ s, $\epsilon_F = -45$ meV, $|\Delta| = 50$ meV, $m_0 = 10$ meV, $m_1 = 20$ meV nm², $v = 30$ meV nm.

are $N_l = 2\sqrt{(\Delta - m_{\mathbf{k}})^2 + v^2k^2} \sin \theta_l$, $N_u = 2\sqrt{(\Delta + m_{\mathbf{k}})^2 + v^2k^2} \cos \theta_u$ with the angles $\theta_{u,l} \in [0, \pi/2]$ defined by $\tan 2\theta_l = vk/[\Delta - m_{\mathbf{k}}]$, $\tan 2\theta_u = vk/[\Delta + m_{\mathbf{k}}]$. The Berry curvature functions for the two bands are

$$\Omega_{\mathbf{k}l}^- = -\frac{v^2(m_0 - m_1k^2 - \Delta)}{2[(\Delta - m_{\mathbf{k}})^2 + v^2k^2]^{\frac{3}{2}}} e_z, \quad (16)$$

$$\Omega_{\mathbf{k}u}^- = \frac{v^2(m_0 - m_1k^2 + \Delta)}{2[(\Delta + m_{\mathbf{k}})^2 + v^2k^2]^{\frac{3}{2}}} e_z.$$

We plot the Berry curvature distribution $\Omega_{\mathbf{k}l}^-$ for $\Delta > 0$ in Fig. 2(b). One can see that $\Omega_{\mathbf{k}}^-$ is even under the inversion of \mathbf{k} so that it possesses a noncentrosymmetric distribution. Therefore, the MnBi₂Te₄ flakes should exhibit the TLMR according to the previous symmetry analysis.

The longitudinal conductivity is contributed by the

electrons near the Fermi surface so that we calculate σ_{xx} in Eq. (8) by inserting the parameters $\mathbf{v}_{\mathbf{k}}$ and $\mathbf{\Omega}_{\mathbf{k}}$ with their values in the relevant band, which is the top valence band here [cf. Fig. 2(a)]. A magnetic field in the z direction that is perpendicular to the flake is assumed. The resistivity is then obtained through the relation $R_{xx} = \sigma_{xx}/(\sigma_{xx}^2 + \sigma_{xy}^2)$ with

$$\sigma_{xy} = \frac{e^2}{(2\pi)^2 \hbar} \sum_{i=u,l,\alpha=\pm} \int d^2\mathbf{k} f_0(\mathbf{k}) (\mathbf{\Omega}_{\mathbf{k}i}^\alpha \cdot \mathbf{e}_z) \quad (17)$$

being the Hall conductivity. The numerical results of R_{xx} as a function of B are plotted in Fig. 2(c), in which the hysteresis effect in accordance with the experimental observation has been taken into account. The up-and-down sweeps of the magnetic field are marked by the arrowed dashed and solid lines, respectively. The coercive field is chosen to be $B_c = 1$ T in the calculation, close to the value in the experiment [22]. The results in Fig. 3(c) clearly show the TLMR with B -scaling, as expected. Here, both σ_{xx} and R_{xx} exhibit linear dependence on B , because the change of σ_{xx} by the magnetic field is small compared with its initial value.

The hysteresis loops in Fig. 2(c) can be understood as follows. Starting with $B < -B_c$, and the ferromagnetic moment is aligned in the same direction with the magnetic field with $\Delta > 0$. As B increases, the system exhibits a TLMR with a positive slope, *i.e.*, $\Delta R_{xx} = R_{xx}(B) - R_{xx}(0) \propto B$ until B reaches the coercive field B_c . In this region, ΔR_{xx} changes its sign as B is inverted, showing nonreciprocity. As B exceeds B_c , Δ undergoes an abrupt flipping to lower the energy of the system, which results in a jump of the MR. Similar discontinuity takes place for the Hall resistance as well, which changes from the quantized value h/e^2 to $-h/e^2$. Both the abrupt changes of the longitudinal MR and the Hall resistance stem from the sign reversal of the Berry curvature. The down sweep [arrowed solid line in Fig. 2(c)] that starts from $B > B_c$ and $\Delta > 0$ can be understood in a similar way. The TLMR feature in Fig. 2(c) obtained by our theory is in good agreement with the experimental observations [22].

Furthermore, we plot the MR for different temperatures in Fig. 2(d) [the exchange field exhibits a very weak temperature dependence below the Néel temperature [57, 58]] and has been chosen to be constant, which exhibit the same features and temperature dependence as those observed in the experiment (see Fig. 2c in Ref. [22]). As a result, the scenario of the TLMR proposed here provides a reasonable and promising explanation for the MR observed in the MnBi_2Te_4 flakes.

V. TLMR IN 3D SPIN-ORBIT-COUPLED ELECTRON GAS

The general scenario of the TLMR is not limited to the 2D systems. To illustrate its universality, in the second

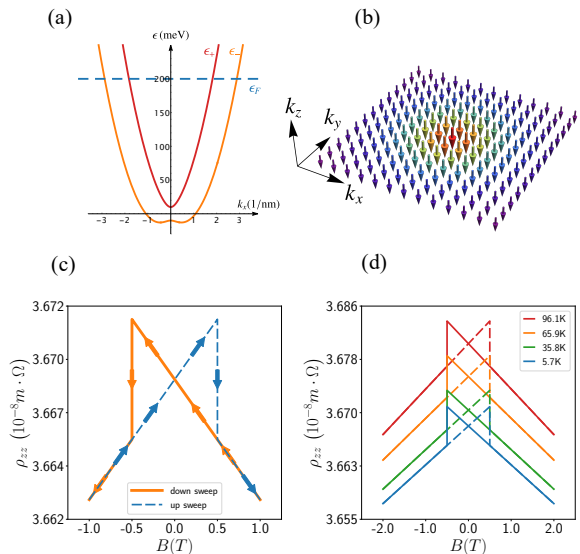


FIG. 3. (Color online). (a) Energy spectra of the spin-orbit coupled electron gas ($k_z = 0, k_y = 0$). The dashed blue line represents the position of the Fermi energy. (b) The distribution of the Berry curvature. (c) The TLMR as a function of the magnetic field at $T = 4.7$ K. The arrowed dashed line represents the up sweep and the arrowed solid line represents the down sweep. (d) TLMR at different temperatures. The relevant parameters are $\tau = 10^{-12}$ s, $\lambda = 40$ meV, $\epsilon_F = 200$ meV, $|\Delta| = 10$ meV.

example we investigate the TLMR in the 3D systems with spin-orbit coupling and a ferromagnetic order. Consider first 3D model with the Rashba effect, which can be realized in BiTeI [59–61]. The corresponding Hamiltonian is

$$H_R = \frac{\hbar^2 k^2}{2m} + \lambda(\mathbf{k} \times \boldsymbol{\sigma}) \cdot \mathbf{e}_z + \Delta \sigma_z, \quad (18)$$

where inversion symmetry is broken along the z -axis, m is the effective mass, the wave vector $\mathbf{k} = (k_x, k_y, k_z)$ consist of three components, λ is the strength of the Rashba spin-orbit coupling, Δ is the Zeeman exchange field due to the ferromagnetic order, and $\boldsymbol{\sigma} = (\sigma_x, \sigma_y, \sigma_z)$ are the Pauli matrices for the spin. Without the exchange field the system possesses the time-reversal symmetry and so cannot exhibit the TLMR.

The energies of the two bands are $\epsilon_{\pm} = \hbar^2 k^2 / 2m \pm \sqrt{\lambda^2(k_x^2 + k_y^2) + \Delta^2}$ as shown in Fig. 3(a), whose corresponding wavefunctions are $|u_{\pm\mathbf{k}}\rangle = [\lambda(ik_x + k_y), \sqrt{\lambda^2(k_x^2 + k_y^2) + \Delta^2}(\cos 2\theta \mp 1)]^T / N_{\pm}$ with the normalization factors $N_+ = 2\sqrt{\Delta^2 + \lambda^2(k_x^2 + k_y^2)} \sin \theta$, $N_- = 2\sqrt{\Delta^2 + \lambda^2(k_x^2 + k_y^2)} \cos \theta$ with the angle $\theta \in [0, \pi/2]$ defined by $\tan 2\theta = \sqrt{\lambda^2(k_x^2 + k_y^2)} / \Delta$. The Berry

curvature distribution of the two bands are

$$\Omega_{\mathbf{k}}^{R\pm} = \mp \frac{\Delta \lambda^2}{2[\Delta^2 + (k_x^2 + k_y^2)\lambda^2]^{\frac{3}{2}}} \mathbf{e}_z. \quad (19)$$

Similar to those in Eq. (16) for the 2D MnBi_2Te_4 , the Berry curvature here contains only the z -component and possesses a noncentrosymmetric distribution as well; see Fig. 3(b) for the distribution of the Berry curvature in a specific k_z plane. The Berry curvature does not rely on k_z so that its noncentrosymmetric distribution in the 3D reciprocal space can be inferred from Fig. 3(b).

We consider the Fermi energy ϵ_F that intersects both bands as shown in Fig. 3(a). Without loss of generality, the electric and magnetic fields are both set to the z -direction. The conductivity σ_{zz} in Eq. (8) is solved numerically taking into account the contributions from both bands. The 3D resistivity $\rho_{zz} = 1/\sigma_{zz}$ is plotted in Fig. 3(c), where we have assumed the existence of a single magnetic domain with a coercive field $B_c^R = 0.5$ T. The numerical results resemble those for the 2D MnBi_2Te_4 flakes, again, consistent with the symmetry analysis in Sec. III. The temperature dependence of the TLMR is shown in Fig. 3(d), which is also similar to the case of the MnBi_2Te_4 [cf. Fig. 2(d)].

Apart from the Rashba-type spin-orbit coupling, the Dresselhaus-type spin-orbit coupling may also exist in 3D systems such as GaAs/AlGaAs quantum wells [62] due to the breaking of the bulk inversion symmetry [63], which can be described by

$$H_D = \frac{\hbar^2 k^2}{2m} + \beta(k_x \sigma_x - k_y \sigma_y) + \Delta \sigma_z, \quad (20)$$

where β is the strength of the Dresselhaus spin-orbit coupling. The two types of spin-orbit coupling result in the same form of the energy spectra (with the replacement $\lambda \rightarrow \beta$) but different spin textures. Accordingly, the Berry curvature for both bands takes the form of

$$\Omega_{\mathbf{k}}^{D\pm} = \pm \frac{\Delta \beta^2}{2[\Delta^2 + (k_x^2 + k_y^2)\beta^2]^{\frac{3}{2}}} \mathbf{e}_z, \quad (21)$$

which is similar to Eq. (19) but with a sign reversal for each band. Given that the sign of the TLMR is determined by the direction of the Berry curvature as indicated in Eq. (9), it can be expected that the TLMR induced by the Dresselhaus spin-orbit coupling possesses the opposite slope compared with that due to the Rashba spin-orbit coupling.

VI. MULTI-DOMAIN STRUCTURES AND DIFFERENCES WITH AMR

In the examples discussed in the previous two sections, we have assumed that the ferromagnetic material possesses a single magnetic domain, which results in the TLMR with the shapes sketched in Figs. 2(c) and 3(c).

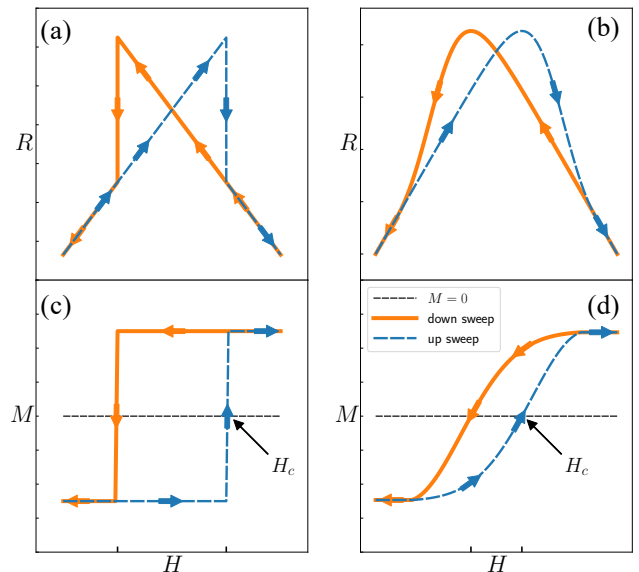


FIG. 4. (Color online). (a) Schematic diagram of the TLMR in the single domain regime with the corresponding hysteresis loop of the magnetization in (c). (b) Schematic diagram of the TLMR in the multi-domain regime with the corresponding hysteresis loop of the magnetization in (d).

Due to the magnetic structure of a single domain, the hysteresis loops of the magnetization exhibits an abrupt flipping as shown in Fig. 4(c), which is responsible for the the discontinuity of the TLMR in Fig. 4(a). For the MnBi_2Te_4 flakes, it is exactly the case and has been verified in the experiment. Meanwhile, in many ferromagnetic materials, multi-domain structures usually arise, which give rise to the conventional hysteresis loop of the magnetization as sketched in Fig. 4(d). Recall that the TLMR here is induced by the Berry curvature configurations which is determined by the (average) magnetization M or equivalently, the Zeeman field Δ in previous discussions. Therefore, it can be inferred that a continuous change of M with the magnetic field H leads to a smooth variation of the Berry curvature as well. Accordingly, the MR is expected to change from the configuration in Fig. 4(a) to that in Fig. 4(b), in which the abrupt jump of the MR disappears. Nevertheless, the linear $B(H)$ -scaling persists for a small magnetic field around zero.

It is worth noting that the LMR with B -scaling has also been reported in a variety of materials like Ge(111) [64, 65] and Co/Pd thin-film [34], the latter possessing the same MR configurations as those in Fig. 4(b). In these materials, the LMR was explained by the conventional anisotropic magnetoresistance (AMR) mechanism [66]. Therefore, it is important to discriminate our scenario of the TLMR in the multi-domain regime from that of the conventional AMR. Physically, the main difference between the TLMR and the AMR is that the former is induced by the joint action of the Berry cur-

vature and the magnetic field while the latter stems directly from the change of the magnetization rather than the magnetic field itself, which possess different manifestations. If the magnetization of the system remains unchanged as the magnetic field varies, which is just the case in the regime of the single magnetic domain as shown in Fig. 4(c) or the saturation magnetization [cf. Fig. 5(b) in Ref. [34] and Fig. 8 in Ref. [67]], the resistivity does not change for the AMR scenario. In stark contrast, the TLMR shows up even if the magnetization remains constant in these regions. However, in the region where the magnetization changes smoothly with the magnetic field, the MR may look similar for both the AMR and TLMR scenarios [compare Figs. 4(b,d) with Fig. 5(b) in Ref. [34] and Fig. 8 in Ref. [67]]. In this case, further analysis of the results beyond such parametric regions is required to discriminate the two scenarios.

VII. TOPOLOGICAL LINEAR THERMOCONDUCTIVITY

So far, we have focused on the effect in the charge transport. Given that the resistivity is a specific type of transport coefficient, the present scenario can be generalized straightforwardly to the other transport coefficients such as the thermoconductivity [68]. Similar to the TLMR, the TLTC can also arise due to the same scenario. Specifically, the z -direction thermoconductivity κ_{zz} is defined by [68–70]

$$\kappa_{zz} = L_{zz}^{22} - L_{zz}^{21}(L_{zz}^{11})^{-1}L_{zz}^{12}, \quad (22)$$

with $L_{zz}^{11} = \sigma_{zz}$ the longitudinal conductivity in Eq. (8) and the other transport coefficients calculated by

$$\begin{aligned} L_{zz}^{21} &= TL_{zz}^{12} = \int \frac{d^3\mathbf{k}}{(2\pi)^3} \frac{e\tau}{D_{\mathbf{k}}} (v_{\mathbf{k}}^z + \frac{e}{\hbar} B^z \mathbf{v}_{\mathbf{k}} \cdot \boldsymbol{\Omega}_{\mathbf{k}})^2 (\epsilon_{\mathbf{k}} - \epsilon_F) \frac{\partial f_0}{\partial \epsilon_{\mathbf{k}}} \\ L_{zz}^{22} &= - \int \frac{d^3\mathbf{k}}{(2\pi)^3} \frac{\tau}{TD_{\mathbf{k}}} (v_{\mathbf{k}}^z + \frac{e}{\hbar} B^z \mathbf{v}_{\mathbf{k}} \cdot \boldsymbol{\Omega}_{\mathbf{k}})^2 (\epsilon_{\mathbf{k}} - \epsilon_F)^2 \frac{\partial f_0}{\partial \epsilon_{\mathbf{k}}}. \end{aligned} \quad (23)$$

We here focus on the elastic scattering in the heat transport which requires a low temperature such that $\tau \simeq \tau_1$. All these transport coefficients possess the similar forms of Eq. (8) and in particular, have the same \mathbf{B} -dependence. Therefore, the symmetry analysis concludes that linear terms in B arise for all the coefficients L_{zz}^{11} , L_{zz}^{12} , L_{zz}^{21} and L_{zz}^{22} as long as the distribution of the Berry curvature is noncentrosymmetric in the reciprocal space. Furthermore, by noting that the linear terms in B of all the transport coefficients is much smaller than the constant terms, the thermoconductivity κ_{zz} also exhibits the B -scaling behavior. In Fig. 5, we plot $\kappa_{zz}(B)/\kappa_{zz}(0)$ as a function of B for MnBi₂Te₄ flakes below the Néel temperature [57, 58], which exhibits linear dependence of B . Our results show that as long as the system is in the TLMR regime, other transport coefficients such as the thermoconductivity also exhibit linear B -dependence.

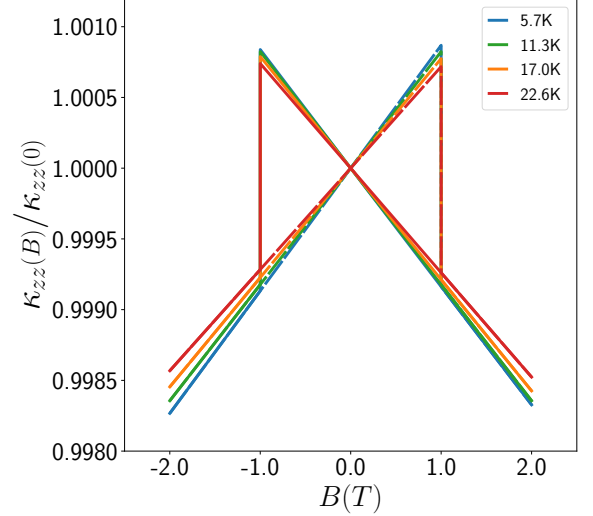


FIG. 5. (Color online). TLTC at different temperatures. The dashed (solid) lines represent up (down) sweep. The relevant parameters are $\tau = 10^{-12}$ s, $\lambda = 40$ meV, $\epsilon_F = -45$ meV, $|\Delta| = 50$ meV, $m_0 = 10$ meV, $m_1 = 20$ meV nm², $v = 30$ meV nm.

VIII. CONCLUDING REMARKS

In conclusion, we have uncovered a general mechanism for the TLMR and TLTC which is induced by the noncentrosymmetric distribution of the Berry curvature. Such effects are predicted to exist in both 2D and 3D systems with nonvanishing Berry curvature. Our theory provides a satisfactory explanation to the existing experiment on the 2D MnBi₂Te₄ flakes [22]. It is also straightforward to explain the same phenomena observed in the 3D magnetic Weyl semimetal Co₃Sn₂S₂ very recently [71]. Actually, Fig. 6 in Ref. [71] resembles Figs. 2(c) and 3(c).

Finally, it is worthwhile to compare our mechanism with those in Refs. [18–20]. Firstly, the LMR in Refs. [18, 19] originates from noncentrosymmetric distribution of the velocity in the reciprocal space while the TLMR here stems from the noncentrosymmetric Berry curvature. Secondly, different from Refs [18–20] that focus on the specific Weyl semimetal, our theory offers a general perspective that can be applied to a wide range of physical systems.

IX. ACKNOWLEDGEMENT

We thank for the helpful discussion with Ming-Xun Deng and Xing-Yu Liu. This work was supported by the National Natural Science Foundation of China under Grant No. 12074172 (W.C.), No. 12222406 (W.C.), No. 12174182 (D.Y.X), No. 12274203 (B.F.M) and No. 12264019 (W.L.), Fundamental Research Funds for the Central Universities(W.C.), the startup grant at Nanjing

University (W.C.), the State Key Program for Basic Researches of China under Grants No. 2021YFA1400403

(D.Y.X.) and the Excellent Programme at Nanjing University.

-
- [1] A. B. Pippard, *Magnetoresistance in metals*, Vol. 2 (Cambridge university press, 1989).
- [2] J. M. Ziman, *Principles of the Theory of Solids* (Cambridge university press, 1972).
- [3] P. A. Lee and T. V. Ramakrishnan, Disordered electronic systems, *Rev. Mod. Phys.* **57**, 287 (1985).
- [4] M. Z. Hasan and C. L. Kane, Colloquium: topological insulators, *Reviews of modern physics* **82**, 3045 (2010).
- [5] X.-L. Qi and S.-C. Zhang, Topological insulators and superconductors, *Reviews of Modern Physics* **83**, 1057 (2011).
- [6] B. Lv, T. Qian, and H. Ding, Experimental perspective on three-dimensional topological semimetals, *Reviews of Modern Physics* **93**, 025002 (2021).
- [7] D. Son and B. Spivak, Chiral anomaly and classical negative magnetoresistance of weyl metals, *Physical Review B* **88**, 104412 (2013).
- [8] A. Burkov, Chiral anomaly and diffusive magnetotransport in weyl metals, *Physical review letters* **113**, 247203 (2014).
- [9] H.-Z. Lu, J. Shi, and S.-Q. Shen, Competition between weak localization and antilocalization in topological surface states, *Phys. Rev. Lett.* **107**, 076801 (2011).
- [10] I. Garate and L. Glazman, Weak localization and antilocalization in topological insulator thin films with coherent bulk-surface coupling, *Phys. Rev. B* **86**, 035422 (2012).
- [11] H.-Z. Lu and S.-Q. Shen, Finite-temperature conductivity and magnetoconductivity of topological insulators, *Phys. Rev. Lett.* **112**, 146601 (2014).
- [12] H.-Z. Lu, S.-B. Zhang, and S.-Q. Shen, High-field magnetoconductivity of topological semimetals with short-range potential, *Physical Review B* **92**, 045203 (2015).
- [13] W. Chen, H.-Z. Lu, and O. Zilberberg, Weak localization and antilocalization in nodal-line semimetals: Dimensionality and topological effects, *Phys. Rev. Lett.* **122**, 196603 (2019).
- [14] G. L. J. A. Rikken, J. Fölling, and P. Wyder, Electrical magnetochiral anisotropy, *Phys. Rev. Lett.* **87**, 236602 (2001).
- [15] V. A. Zyuzin, Linear magnetoconductivity in magnetic metals, *Phys. Rev. B* **104**, L140407 (2021).
- [16] C. Xiao, H. Chen, Y. Gao, D. Xiao, A. H. MacDonald, and Q. Niu, Linear magnetoresistance induced by intrascattering semiclassicals of bloch electrons, *Phys. Rev. B* **101**, 201410 (2020).
- [17] T. Morimoto and N. Nagaosa, Chiral anomaly and giant magnetochiral anisotropy in noncentrosymmetric weyl semimetals, *Phys. Rev. Lett.* **117**, 146603 (2016).
- [18] D. Ma, H. Jiang, H. Liu, and X. Xie, Planar hall effect in tilted weyl semimetals, *Physical Review B* **99**, 115121 (2019).
- [19] K. Das and A. Agarwal, Linear magnetochiral transport in tilted type-i and type-ii weyl semimetals, *Phys. Rev. B* **99**, 085405 (2019).
- [20] Z. Zhang, Y. Liu, and W. Duan, Berry-curvature-induced linear magnetotransport in magnetic weyl semimetals, arXiv preprint arXiv:2207.13233 (2022).
- [21] C.-Z. Chang, J. Zhang, X. Feng, J. Shen, Z. Zhang, M. Guo, K. Li, Y. Ou, P. Wei, L.-L. Wang, *et al.*, Experimental observation of the quantum anomalous hall effect in a magnetic topological insulator, *Science* **340**, 167 (2013).
- [22] Y. Deng, Y. Yu, M. Z. Shi, Z. Guo, Z. Xu, J. Wang, X. H. Chen, and Y. Zhang, Quantum anomalous hall effect in intrinsic magnetic topological insulator mnbi₂te₄, *Science* **367**, 895 (2020).
- [23] J. Feng, Y. Pang, D. Wu, Z. Wang, H. Weng, J. Li, X. Dai, Z. Fang, Y. Shi, and L. Lu, Large linear magnetoresistance in dirac semimetal cd₃as₂ with fermi surfaces close to the dirac points, *Phys. Rev. B* **92**, 081306 (2015).
- [24] T. Liang, Q. Gibson, M. N. Ali, M. Liu, R. Cava, and N. Ong, Ultrahigh mobility and giant magnetoresistance in the dirac semimetal cd₃as₂, *Nature materials* **14**, 280 (2015).
- [25] M. Novak, S. Sasaki, K. Segawa, and Y. Ando, Large linear magnetoresistance in the dirac semimetal tlbisse, *Phys. Rev. B* **91**, 041203 (2015).
- [26] A. Narayanan, M. D. Watson, S. F. Blake, N. Bruyant, L. Drigo, Y. L. Chen, D. Prabhakaran, B. Yan, C. Felser, T. Kong, P. C. Canfield, and A. I. Coldea, Linear magnetoresistance caused by mobility fluctuations in *n*-doped cd₃as₂, *Phys. Rev. Lett.* **114**, 117201 (2015).
- [27] Y. Zhao, H. Liu, C. Zhang, H. Wang, J. Wang, Z. Lin, Y. Xing, H. Lu, J. Liu, Y. Wang, S. M. Brombosz, Z. Xiao, S. Jia, X. C. Xie, and J. Wang, Anisotropic fermi surface and quantum limit transport in high mobility three-dimensional dirac semimetal cd₃as₂, *Phys. Rev. X* **5**, 031037 (2015).
- [28] H. Tang, D. Liang, R. L. Qiu, and X. P. Gao, Two-dimensional transport-induced linear magneto-resistance in topological insulator bi₂se₃ nanoribbons, *ACS nano* **5**, 7510 (2011).
- [29] C. M. Wang and X. L. Lei, Linear magnetoresistance on the topological surface, *Phys. Rev. B* **86**, 035442 (2012).
- [30] X. Wang, Y. Du, S. Dou, and C. Zhang, Room temperature giant and linear magnetoresistance in topological insulator bi₂te₃ nanosheets, *Phys. Rev. Lett.* **108**, 266806 (2012).
- [31] A. A. Abrikosov, Quantum magnetoresistance, *Phys. Rev. B* **58**, 2788 (1998).
- [32] J. Feng, Y. Pang, D. Wu, Z. Wang, H. Weng, J. Li, X. Dai, Z. Fang, Y. Shi, and L. Lu, Large linear magnetoresistance in dirac semimetal cd₃as₂ with fermi surfaces close to the dirac points, *Phys. Rev. B* **92**, 081306 (2015).
- [33] J. G. Checkelsky, J. Ye, Y. Onose, Y. Iwasa, and Y. Tokura, Dirac-fermion-mediated ferromagnetism in a topological insulator, *Nature Physics* **8**, 729 (2012).
- [34] D. A. Gilbert, B. B. Maranville, A. L. Balk, B. J. Kirby, P. Fischer, D. T. Pierce, J. Unguris, J. A. Borchers, and K. Liu, Realization of ground-state artificial skyrmion lattices at room temperature, *Nature communications* **6**,

- 1 (2015).
- [35] M. Parish and P. Littlewood, Non-saturating magnetoresistance in heavily disordered semiconductors, *Nature* **426**, 162 (2003).
- [36] D. Xiao, M.-C. Chang, and Q. Niu, Berry phase effects on electronic properties, *Reviews of modern physics* **82**, 1959 (2010).
- [37] D. Xiao, J. Shi, and Q. Niu, Berry phase correction to electron density of states in solids, *Physical review letters* **95**, 137204 (2005).
- [38] C. Duval, Z. Horváth, P. A. Horvathy, L. Martina, and P. Stichel, Berry phase correction to electron density in solids and "exotic" dynamics, *Modern Physics Letters B* **20**, 373 (2006).
- [39] N. Nagaosa, J. Sinova, S. Onoda, A. H. MacDonald, and N. P. Ong, Anomalous hall effect, *Reviews of modern physics* **82**, 1539 (2010).
- [40] X. Dai, Z. Z. Du, and H.-Z. Lu, Negative magnetoresistance without chiral anomaly in topological insulators, *Phys. Rev. Lett.* **119**, 166601 (2017).
- [41] N. Armitage, E. Mele, and A. Vishwanath, Weyl and dirac semimetals in three-dimensional solids, *Reviews of Modern Physics* **90**, 015001 (2018).
- [42] M.-C. Chang and M.-F. Yang, Chiral magnetic effect in a two-band lattice model of weyl semimetal, *Physical Review B* **91**, 115203 (2015).
- [43] M. Stephanov and Y. Yin, Chiral kinetic theory, *Physical review letters* **109**, 162001 (2012).
- [44] S.-Q. Shen, Spin hall effect and berry phase in two-dimensional electron gas, *Phys. Rev. B* **70**, 081311 (2004).
- [45] G. Sundaram and Q. Niu, Wave-packet dynamics in slowly perturbed crystals: Gradient corrections and berry-phase effects, *Phys. Rev. B* **59**, 14915 (1999).
- [46] N. Ashcroft and N. Mermin, *Solid state physics (saunders college, philadelphia)*, *Solid state Physics* **1** (1976).
- [47] X. Huang, L. Zhao, Y. Long, P. Wang, D. Chen, Z. Yang, H. Liang, M. Xue, H. Weng, Z. Fang, X. Dai, and G. Chen, Observation of the chiral-anomaly-induced negative magnetoresistance in 3d weyl semimetal taas, *Phys. Rev. X* **5**, 031023 (2015).
- [48] N. Ong and S. Liang, Experimental signatures of the chiral anomaly in dirac-weyl semimetals, *Nature Reviews Physics* **3**, 394 (2021).
- [49] M.-C. Chang and Q. Niu, Berry phase, hyperorbits, and the hofstadter spectrum: Semiclassical dynamics in magnetic bloch bands, *Phys. Rev. B* **53**, 7010 (1996).
- [50] H. K. Pal and D. L. Maslov, Necessary and sufficient condition for longitudinal magnetoresistance, *Phys. Rev. B* **81**, 214438 (2010).
- [51] M.-X. Yang, H. Geng, W. Luo, L. Sheng, W. Chen, and D. Y. Xing, Sign reversal of magnetoresistivity in massive nodal-line semimetals due to the lifshitz transition of the fermi surface, *Phys. Rev. B* **104**, 165149 (2021).
- [52] N. Nagaosa, T. Morimoto, and Y. Tokura, Transport, magnetic and optical properties of weyl materials, *Nature Reviews Materials* **5**, 621 (2020).
- [53] J. Li, Y. Li, S. Du, Z. Wang, B.-L. Gu, S.-C. Zhang, K. He, W. Duan, and Y. Xu, Intrinsic magnetic topological insulators in van der waals layered mnbi2te4-family materials, *Science Advances* **5**, eaaw5685 (2019).
- [54] P. M. Sass, W. Ge, J. Yan, D. Obeysekera, J. Yang, and W. Wu, Magnetic imaging of domain walls in the antiferromagnetic topological insulator mnbi2te4, *Nano Letters* **20**, 2609 (2020).
- [55] H. Fu, C.-X. Liu, and B. Yan, Exchange bias and quantum anomalous hall effect in the mnbi2te4/cr3 heterostructure, *Science advances* **6**, eaaz0948 (2020).
- [56] J. Wang, B. Lian, and S.-C. Zhang, Universal scaling of the quantum anomalous hall plateau transition, *Phys. Rev. B* **89**, 085106 (2014).
- [57] Y. Deng, Y. Yu, M. Z. Shi, Z. Guo, Z. Xu, J. Wang, X. H. Chen, and Y. Zhang, Quantum anomalous hall effect in intrinsic magnetic topological insulator mnbi2te4, *Science* **367**, 895 (2020).
- [58] M. M. Otrokov, I. I. Klimovskikh, H. Bentmann, D. Estyunin, A. Zeugner, Z. S. Aliev, S. Gaß, A. Wolter, A. Koroleva, A. M. Shikin, *et al.*, Prediction and observation of an antiferromagnetic topological insulator, *Nature* **576**, 416 (2019).
- [59] M. B. Bahramy, R. Arita, and N. Nagaosa, Origin of giant bulk rashba splitting: Application to bitei, *Physical Review B* **84**, 041202 (2011).
- [60] K. Ishizaka, M. Bahramy, H. Murakawa, M. Sakano, T. Shimojima, T. Sonobe, K. Koizumi, S. Shin, H. Miyahara, A. Kimura, *et al.*, Giant rashba-type spin splitting in bulk bitei, *Nature materials* **10**, 521 (2011).
- [61] H. Murakawa, M. Bahramy, M. Tokunaga, Y. Kohama, C. Bell, Y. Kaneko, N. Nagaosa, H. Hwang, and Y. Tokura, Detection of berry's phase in a bulk rashba semiconductor, *Science* **342**, 1490 (2013).
- [62] M. Studer, M. Walser, S. Baer, H. Rusterholz, S. Schön, D. Schuh, W. Wegscheider, K. Ensslin, and G. Salis, Role of linear and cubic terms for drift-induced dresselhaus spin-orbit splitting in a two-dimensional electron gas, *Physical Review B* **82**, 235320 (2010).
- [63] G. Dresselhaus, Spin-orbit coupling effects in zinc blende structures, *Physical Review* **100**, 580 (1955).
- [64] T. Guillet, C. Zucchetti, Q. Barbedienne, A. Marty, G. Isella, L. Cagnon, C. Vergnaud, H. Jaffrès, N. Reyren, J.-M. George, A. Fert, and M. Jamet, Observation of large unidirectional rashba magnetoresistance in ge(111), *Phys. Rev. Lett.* **124**, 027201 (2020).
- [65] T. Guillet, A. Marty, C. Vergnaud, M. Jamet, C. Zucchetti, G. Isella, Q. Barbedienne, H. Jaffrès, N. Reyren, J.-M. George, and A. Fert, Large rashba unidirectional magnetoresistance in the fe/ge(111) interface states, *Phys. Rev. B* **103**, 064411 (2021).
- [66] T. McGuire and R. Potter, Anisotropic magnetoresistance in ferromagnetic 3d alloys, *IEEE Transactions on Magnetics* **11**, 1018 (1975).
- [67] W. Gil, D. Görlitz, M. Horisberger, and J. Kötzler, Magnetoresistance anisotropy of polycrystalline cobalt films: Geometrical-size and domain effects, *Phys. Rev. B* **72**, 134401 (2005).
- [68] D. Xiao, Y. Yao, Z. Fang, and Q. Niu, Berry-phase effect in anomalous thermoelectric transport, *Phys. Rev. Lett.* **97**, 026603 (2006).
- [69] R. Lundgren, P. Laurell, and G. A. Fiete, Thermoelectric properties of weyl and dirac semimetals, *Phys. Rev. B* **90**, 165115 (2014).
- [70] B. Jiang, J. Zhao, J. Qian, S. Zhang, X. Qiang, L. Wang, R. Bi, J. Fan, H.-Z. Lu, E. Liu, and X. Wu, Antisymmetric seebeck effect in a tilted weyl semimetal, *Phys. Rev. Lett.* **129**, 056601 (2022).
- [71] A. G. Moghaddam, K. Geishendorf, R. Schlitz, J. I. Facio, P. Vir, C. Shekhar, C. Felser, K. Nielsch, S. T. Goennenwein, J. van den Brink, *et al.*, Observation of an un-

expected negative magnetoresistance in magnetic weyl

semimetal $\text{Co}_3\text{Sn}_2\text{S}_2$, *Materials Today Physics*, 100896 (2022).